MIT Spring 2008, Course Project for
18.086 Computational Science and Engineering II

Finite Difference Modeling of Micro Optofluidic Switch by solving 2-D Navier-Stokes Equations

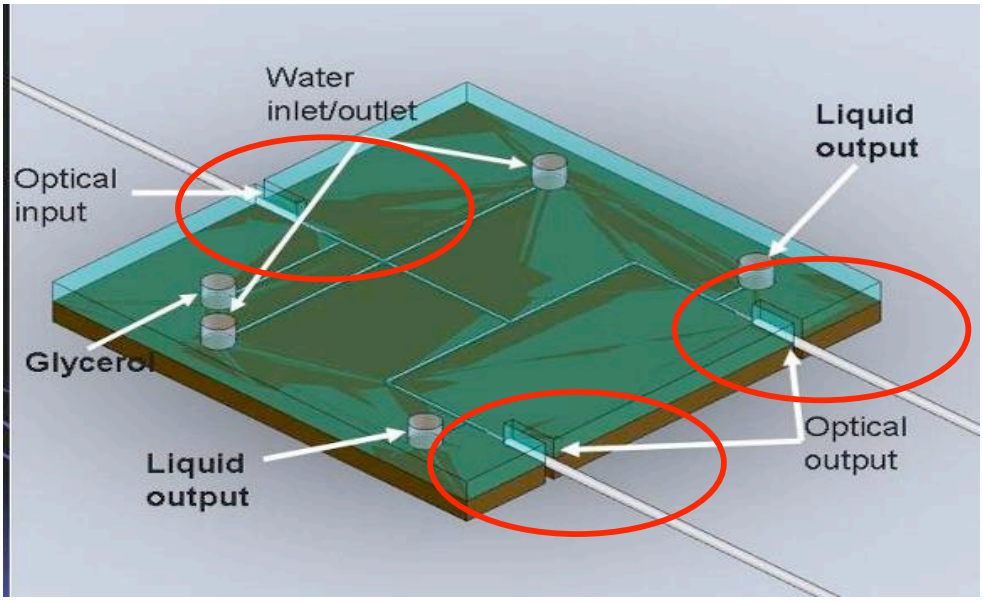

Tian Fook Kong
tianfook@mit.edu

Abstract

In this report, we present a finite difference framework to simulate the switching behavior of a micro optofluidic switch by solving the 2-D Navier-Stokes equations. The switching response time was found to be dependent on the flow condition. We observed that the ratio between the velocities of the two sheath streams of a one-phase flow required for switching is about $2.15:1$. The fastest switching speed for the system was found to be about 3 millisecond (167Hz). For visualization of the flow, we have incorporated fluorescent dye in the core stream using the particle method.

In addition, we have shown the working principle of a microfluidic signal generator. The core width ratio, which determines the magnitude of the signal received by optical fiber at the channel outlet, could be changed dynamically by manipulating the core and sheath stream flow rates. We have not, however, implemented a two-phase flow, unstructured meshes, time-dependent geometries, non-constant density or turbulence models.

Acknowledgement

I would like to take this opportunity to express my sincere gratitude to Dr. Benjamin Seibold for his tutelage and advice in guiding the student towards completing this course project. He has been very patient in explaining the approach and strategy used in this project.

In addition, I am also grateful to Mr. Chun Fan Goh for the collaboration work on understanding the staggered grid and 2-D Navier-Stokes solver written by Dr. Benjamin Seibold for the Computational Science and Engineering II course.

Lastly, I would also like to extend my appreciation to Associate Professor Nguyen Nam Trung for introducing me to the exciting field of microfluidics. I developed a microfluidic switch together with him during my final year project at Nanyang Technological University, Singapore.

Table of Contents

CHAPTER 1

Introduction

1.1 Microfluidic Switch

Microfluidics is a branch of the fluid mechanics field that deals with micro-liter or nano-liter volumes of fluids. Due to the miniature nature of microfluidics, the flow in the microchannel (with a low Reynolds number) is essentially laminar. In the two-way optical switch design shown in Figure 1-1, the glycerol core inlet with two water side-streams forms a three-layer laminar water-glycerol-water flow.

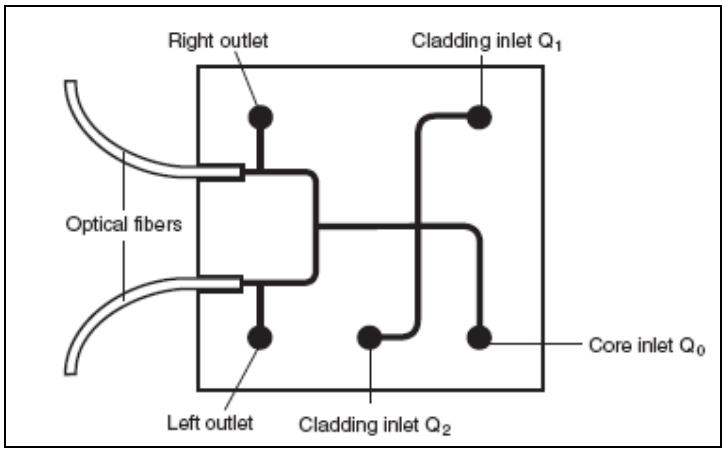

Figure 1-1: Configuration of the two-way optical switch microchannel [1]

The optofluidic switch [1] is made possible by the speed differential between the two water side-streams. Figure 1-2(a) shows the laminar flow formed in the microchannel when the water side-streams are flowing into the microchannel at an identical flow rate. The core flow is being "switched" either up or down (Figure 1-2(b)-(c)) by having one of flow rates substantially higher than the other.

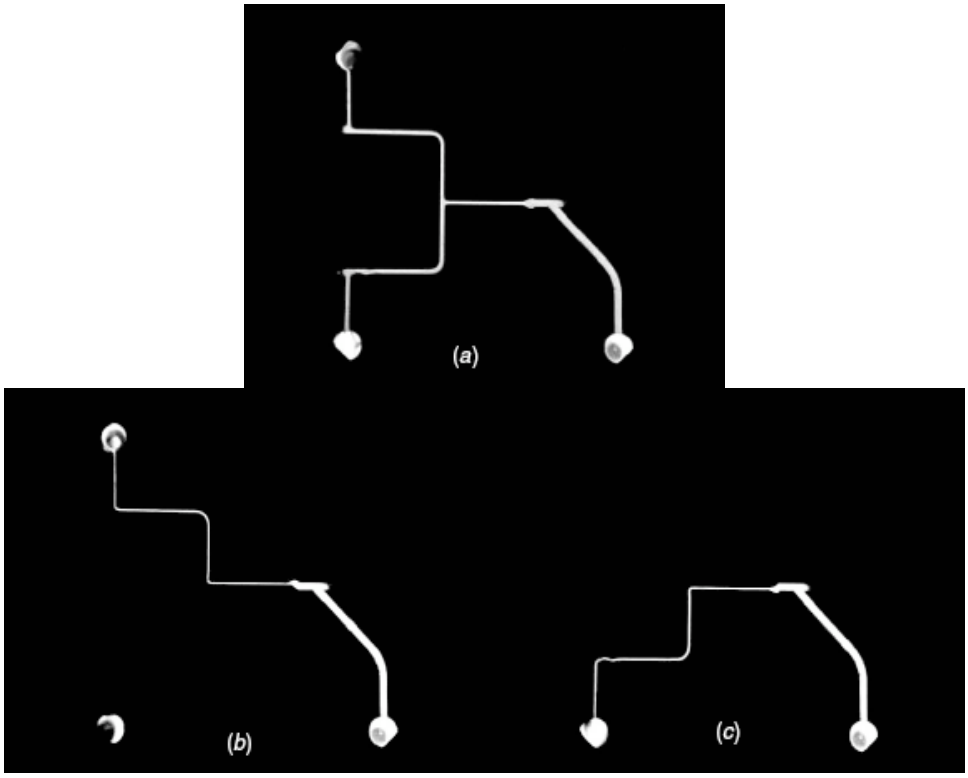

Figure 1-2: Fluorescent image of the core stream at different conditions: (a) splitting (b) up switching (c) down switching. [1]

1.2 Hydrodynamic Focusing

The model presented in [2] has considered a three-layer laminar flow, namely one sample stream sandwiched between two identical sheath streams. Two assumptions were made: uniform velocities in all three immiscible streams and two identical sheath streams. A two-phase Navier-Stokes equation system was used to describe the system, and the effect of different viscosities was considered. An analytical model of hydrodynamic focusing for actual geometry and dimensionless model is shown in Figure 1-3. The width ratio, r, is defined as the ratio of the width occupied by the core stream to the width of the channel.

Note: Equations and Figures found in Section 1.2, Hydrodynamic Focusing, are extracted from [2]

The velocity distribution u_1 and u_2 in the channel can be described by the Navier-Stokes equation as follows:

$$\frac{\partial^2 u_1}{\partial y^2} + \frac{\partial^2 u_1}{\partial z^2} = \frac{1}{\eta_1}\frac{\partial p}{\partial x}, \frac{\partial^2 u_2}{\partial y^2} + \frac{\partial^2 u_2}{\partial z^2} = \frac{1}{\eta_2}\frac{\partial p}{\partial x}. \quad (1)$$

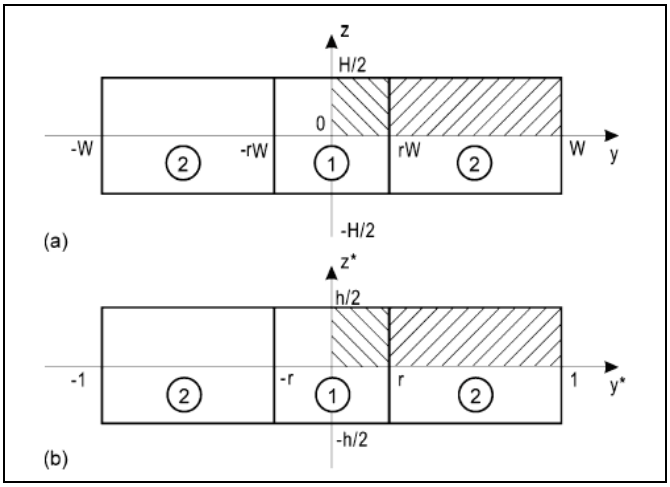

Figure 1-3: Analytical model of hydrodynamic focusing: (a) actual geometry, (b) the dimensionless model.

Non-dimensionalizing the velocity by a reference velocity u_0 and the coordinates by W yield the following [2]:

$$\frac{\partial^2 u_1^*}{\partial y^{*2}} + \frac{\partial^2 u_1^*}{\partial z^{*2}} = \frac{W}{\eta_1 u_o}\frac{\partial p}{\partial x^*}, \frac{\partial^2 u_2^*}{\partial y^{*2}} + \frac{\partial^2 u_2^*}{\partial z^{*2}} = \frac{W}{\eta_2 u_o}\frac{\partial p}{\partial x^*}. \quad (2)$$

By solving the equation (2) with non-slip and symmetry conditions, the width ratio, *r*, can be determined by using the equation below:

$$r = \frac{1}{1 + 2\beta\kappa}, \quad (3)$$

where $\kappa = \frac{Q_{sideflow}}{Q_{core}}$ and $\beta = \frac{\eta_{sideflow}}{\eta_{core}}$.

Note: Equations and Figures found in Section 1.2, Hydrodynamic Focusing, are extracted from [2]

As such, the core width can be manipulated by changing the flow ratio, κ. The core width will increase when the flow rate of the core, Q_{core}, is increased, while keeping the side stream flow rates, $Q_{sideflow}$, constant.

1.3 Motivation

The fastest switching speed obtained experimentally by Nguyen et al. [1] is 300 milliseconds. However, the switching speed is restricted by the reaction time of the external syringe pumps. The switching behaviors of the microfluidic switch may not be easily observed experimentally due to the physical constraint of the experimental setup. Therefore, we implemented a finite difference scheme to simulate the switching behaviors for various flow conditions. In addition, the ratio between the velocities of the two sheath streams required for switching can be determined exactly through simulation.

1.4 Report Organization

Chapter 2 presents our finite difference model of the incompressible Navier-Stokes equations. The numerical discretization performed on a staggered grid for the pressure, horizontal velocity component, and vertical velocity component is described in detail in this chapter. The treatment of boundary conditions is also described. Particles are inserted into the domain for visualization purposes.

Chapter 3 discusses the results obtained from the model. First, the flow velocity profile and pressure distribution for a straight channel are presented. Subsequently, we discuss the results obtained for the microfluidic switch model. The switching response time and speed differential required for switching are also investigated in detail in this chapter. The working principle and results for a microfluidic signal generator is also presented. Lastly, the report concludes with recommendation for future work.

CHAPTER 2

Finite Difference Approach for the 2-D Incompressible Navier-Stokes Equations

2.1 Incompressible Navier-Stokes Equation [3]

The governing equations for incompressible viscous flow are given by the Navier-Stokes equation. The Navier-Stokes and Continuity equations are $\frac{\partial \vec{u}}{\partial t} + (\vec{u}.\nabla)\vec{u} = -\nabla p + \frac{1}{\mathrm{Re}}\Delta\vec{u} + \vec{f}$, and $\nabla.\vec{u} = 0$. In a 2-D incompressible flow, these two equations can be further simplified to:

$$\begin{aligned} u_t + p_x &= -(u^2)_x - (uv)_y + \frac{1}{\mathrm{Re}}(u_{xx} + u_{yy}), \\ u_t + p_y &= -(uv)_x - (u^2)_y + \frac{1}{\mathrm{Re}}(v_{xx} + v_{yy}), \\ u_x + v_y &= 0. \end{aligned} \tag{1}$$

2.2 Reynolds Number

The Reynolds number, which is defined to be the ratio of inertial forces to the viscous forces, is given by:

$$\mathrm{Re} = \frac{uL}{\nu} \tag{2}$$

where u=characteristic velocity, L=characteristic length, and ν=kinematics' viscosity. For this project, the fluid (water) flow rates are typically in the region of $1000\mu l/hr$ ($\approx 0.01235 ms^{-1}$), and the typical characteristic length is $150\mu m$. The dynamic viscosity of water is 10^{-6}. Hence, the Reynolds number obtained for this system is about 1.85.

2.3 Staggered Grid

The numerical discretization is performed on a staggered grid for the pressure, horizontal velocity component, and vertical velocity component (shown in Figure 2-1). The pressure P is placed in the cell center. The horizontal velocity component U is placed in the vertical cell interfaces while the vertical velocity component V is placed in the horizontal cell interfaces. Staggered grid is implemented to avoid checkerboard solution for the pressure.

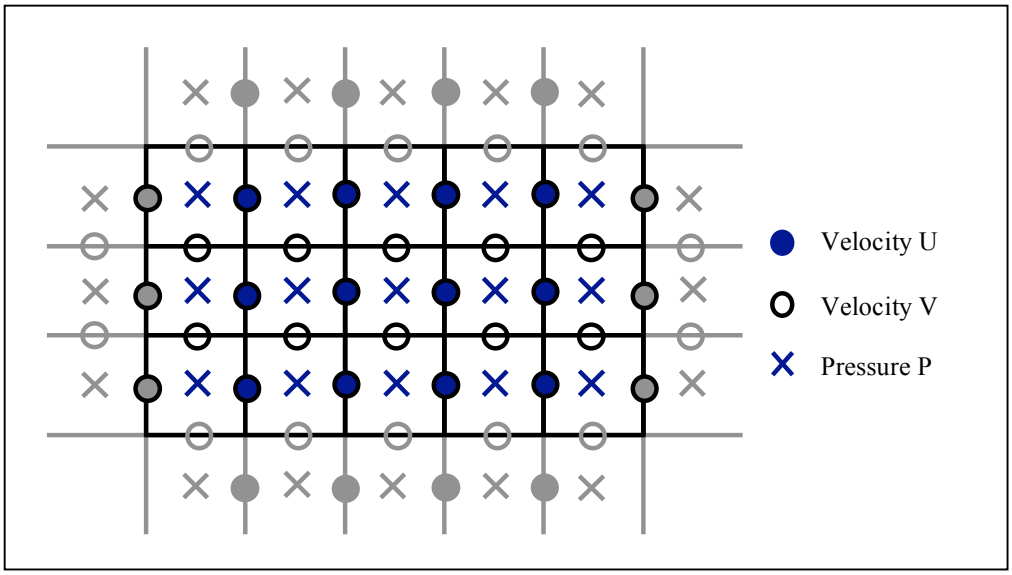

Figure 2-1 Staggered grid with boundary cells [3]

2.4 Boundary Conditions

The flow domain's boundary conditions are shown in Figure 2-2. The no slip conditions: $u = 0, v = 0, \frac{\partial p}{\partial n} = 0$ are applied to all walls in the domain. Dirichlet conditions are used for the velocities U and V at the three water inlets, while Neumann conditions are used for the pressure P as the velocity profiles at the inlets are known. For the two water outlets, Neumann condition is used for the horizontal velocity U and vertical velocity V since these velocities are dependent on the upstream flow conditions. Dirichlet conditions are used for

the pressure P at these two outlets (pressure at the outlets are set to be an arbitrary constant).

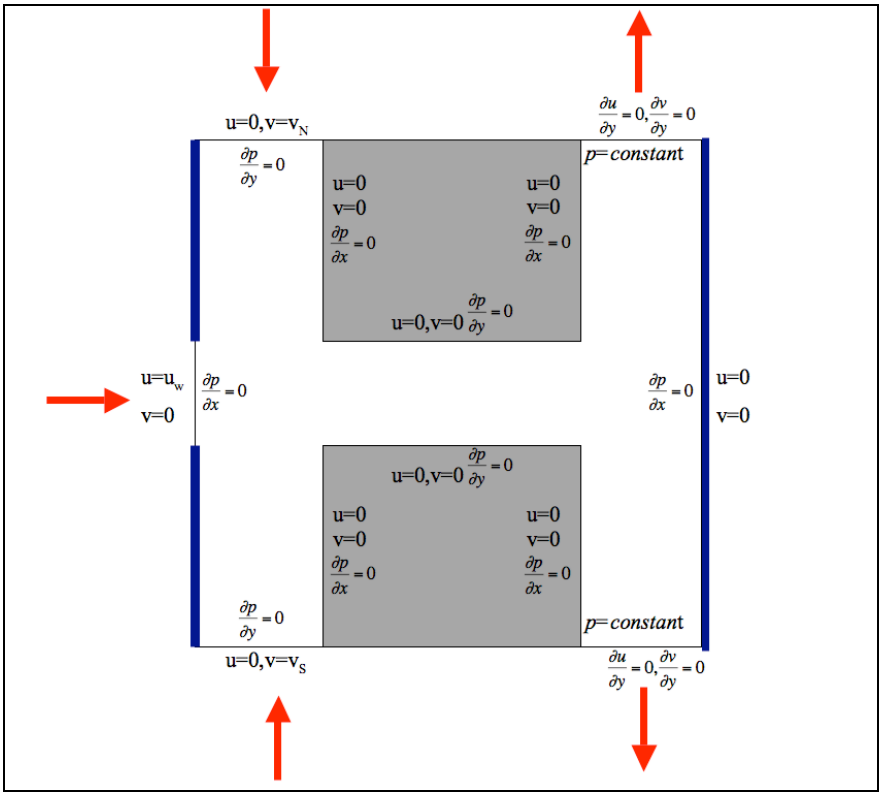

Figure 2-2 Boundary conditions for the flow domain. No slip condition is enforced on all the walls. Since the inlet velocities profiles are known, the three water inlets on the left have Dirichlet boundary conditions for the horizontal and vertical velocity, and Neumann boundary condition for the pressure. The two outlets have Neumann condition for the velocities since the velocity profiles at the outlet are dependent on the inlet flow conditions.

2.5 Building the Laplacian Matrices

The Matlab commands to build the Laplacian Matrices of U, V, and P for the domain without the two blocked region are shown in Figure 2-3.

```
%-----------------------------------------------
%              U velocity Laplacian
%-----------------------------------------------
Uxx = kron(speye(ny),K1(nx-1,hx,2,2));
Uyy = kron(K1(ny,hy,1,1),speye(nx-1));

%-----------------------------------------------
%              V velocity Laplacian
%-----------------------------------------------
Vxx = kron(speye(ny-1),K1(nx,hx,3,3));
Vyy = kron(K1(ny-1,hy,1,1),speye(nx));

%-----------------------------------------------
%              P Pressure Laplacian
%-----------------------------------------------
Pxx = kron(speye(ny),K1(nx,hx,1,1));
Pyy = kron(K1(ny,hy,3,3),speye(nx));

function A = K1(n,h,a11,a22)
% a11: Neumann=1, Dirichlet=2, Dirichlet mid=3;
A = spdiags([-1 a11 0;ones(n-2,1)*[-1 2 -1];0 a22 -1],-1:1,n,n)'/h^2;
```

Figure 2-3 Matlab command for building the Laplacian matrices of U, V, and P

However, in order to include the two blocked region into the domain, the Laplacian matrix for U, V, and P have to be modified. The entries for those points in the blocked region are set to value one on the diagonal and value zero on the off-diagonals. This is to ensure that the pressure and velocities in the flow region are not affected by the values in the blocked region.

In addition, the entries for the points adjacent to the blocked region need to be treated according to the boundary conditions (mid-point Dirichlet or Dirichlet). In Figure 2-4, the points in the green boxes have to be modified. The points at the top and bottom inlets also

need modification since there are mixed boundary conditions for the top and bottom boundaries. The inlets have Dirichlet condition while the outlets have Neumann condition.

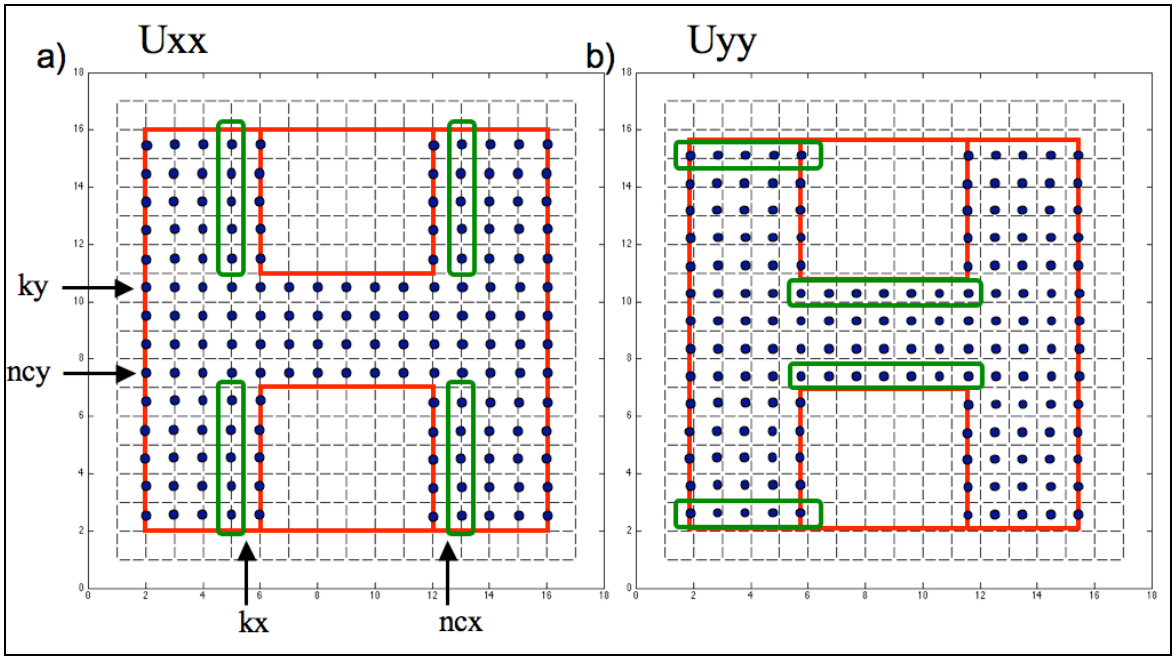

Figure 2-4 Components of the Laplacian matrix of U ($L_u = U_{xx} + U_{yy}$). The entries in U_{xx} and U_{yy} for the grid points located inside the green boxes need to be modified according to the boundary condition at those points. The entries for points in the top and bottom inlets also have to be modified since there are mixed boundary conditions at the top and bottom boundary (Dirichlet for the inlets and Neumann for the outlets). Similar modifications are also necessary for the vertical velocity and pressure Laplacian matrix.

2.6 Flow Visualization

Particle method is used for the flow visualization. Particles (points) are inserted into the domain and removed as the particles exit the domain. The position of the particles are updated using the velocity profile at every time step using:

$$\begin{aligned} x &= x_0 + U * dt * C \\ y &= y_0 + V * dt * C \end{aligned} \tag{3}$$

where $C = \frac{U}{L}$ scales the particle speed to the actual speed.

CHAPTER 3

Results and Discussion

3.1 Duct Flow (Straight Channel)

I have modified the mit18086_navierstokes.m [3] code to model a straight channel flow to gain confidence in dealing with finite difference approach for a 2-D incompressible Navier Stokes flow.

Figure 3-1 shows the pressure and velocity distribution of duct channel for uniform inlet velocity profile. This image is taken after one time step. The pressure is decreasing uniformly downstream. The velocity is pointing to the right as expected.

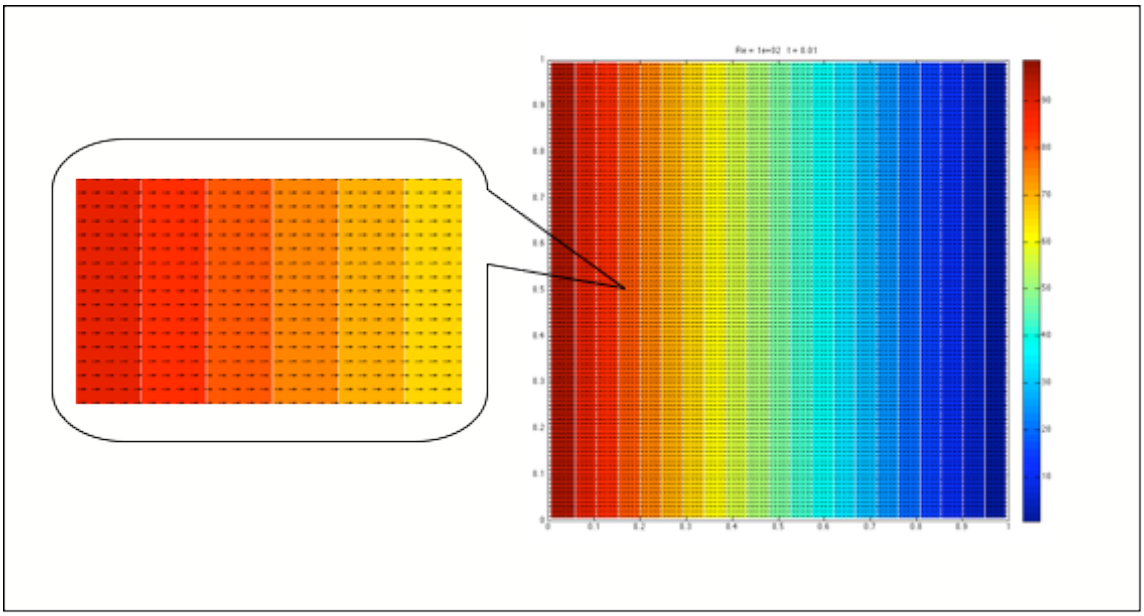

Figure 3-1. Duct Flow Pressure and Velocity Distribution

3.1.1 Effect of Magnitude of Reynolds Number

Reynolds number affects the nature of the flow. The higher the Reynolds number, the more unsteady the flow. Figure 3-2 shows the flow profile for low, medium and high Reynolds number.

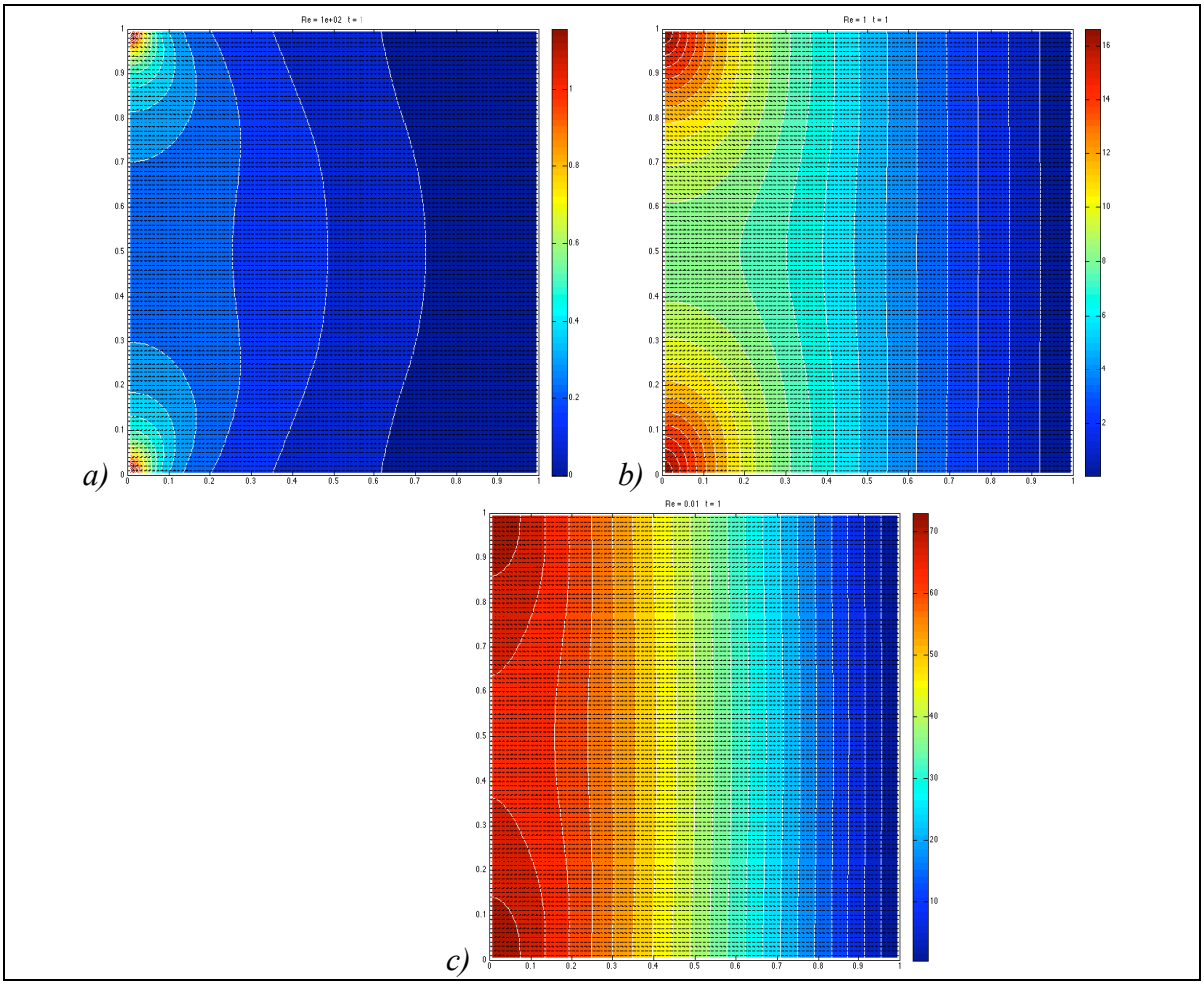

Figure 3-2. Effect of Reynolds number on flow profile a) Re=100 b) Re=1 c) Re=0.01. The higher the Reynolds number, the more unsteady the flow becomes.

3.1.2 Effect of Channel Width-Length Ratio

Figure 3-3 shows the effect of channel width-length ratio. For long channel (low width-length ratio), the downstream pressure varies gradually while a tall thin channel downstream pressure does not vary uniformly.

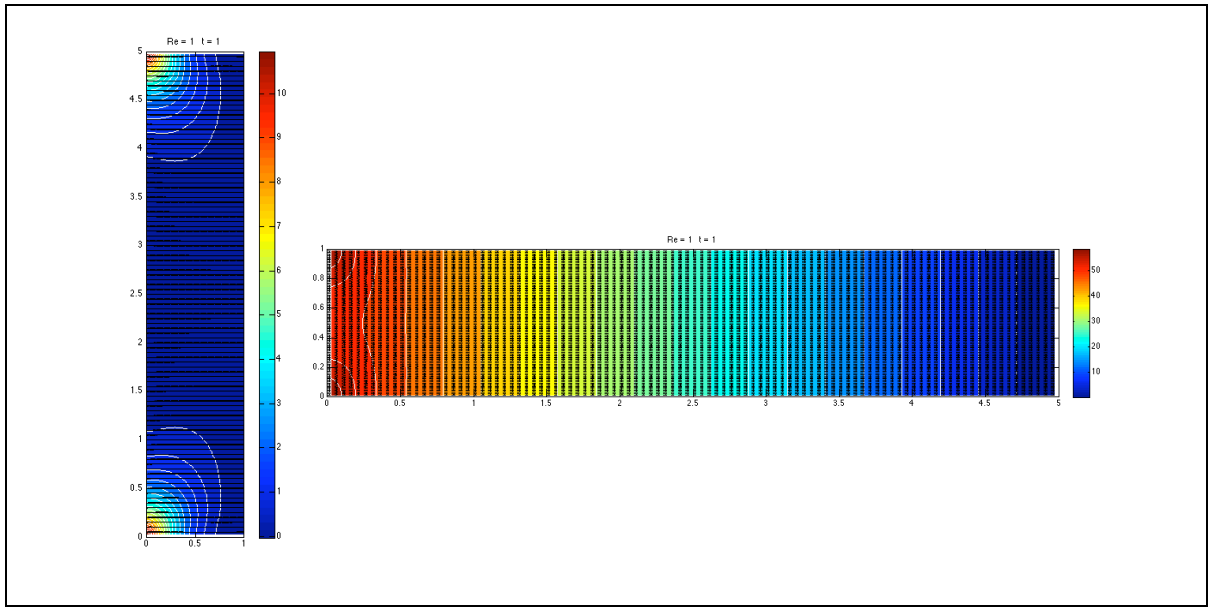

Figure 3-3. Effect of channel width-length ratio. The downstream pressure decreases gradualy for long channel.

3.1.3 Effect of Inlet Velocity Profile

The inlet velocity profile determines the flow profile in a duct. Figure 3-4 shows the flow profiles for uniform, parabolic, upper triangular, upper lower triangular, and staggered inlet velocities. The downstream pressure is set to zero since the solution is only correct up to a constant. Therefore, a pressure of zero would represent the atmospheric pressure.

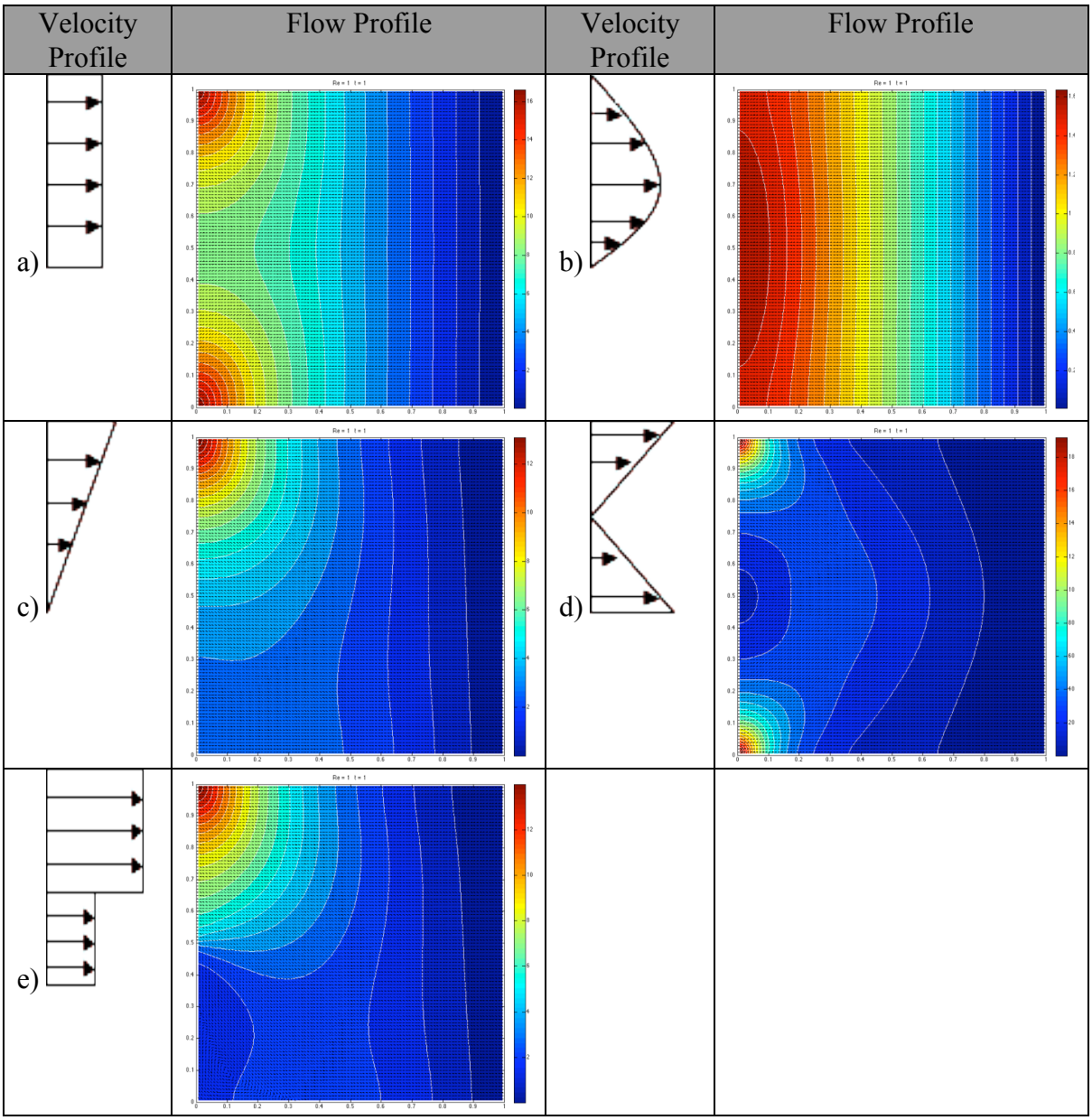

Figure 3-4. Effect of Inlet Velocity Profile: a) uniform, b) parabolic, c) upper triangular, d) upper and lower triangular, and e) staggered velocity profiles

3.2 Microfluidic Switch

In this section, I present the results I have obtained for the microfluidic switch model. The comparison between experimental results with the simulation results for the three cases: a) splitting, b) switched up, and c) switched down are shown in Figure 3-5. The simulation domain is shown in red box found in Figure 3-5(a). Note that the experimental results are obtained using a two-phase flow of water-glycerol-water, while the simulation results are for one-phase flow of three-layer laminar flow of water.

3.2.1 Critical Flow Rate Ratio Between the Side Streams

The core flow is being "switched" either up or down by having one of flow rates substantially higher than the other. The critical flow rate ratio between the side streams is defined as the minimum ratio between the flow rates of water side streams such that the core fluid turned completely into one direction. Simulation results show that for one-phase water flow, $\mathrm{Re} = 2$, and core speed $U = 1$, the critical switching flow rate ratio is 2:15:1.

The experimentally the critical switching flow rate was 10:1. This is because in the experiment was done for a two-phase flow of water-glycerol-water. In the theoretical model given in [1] for the critical switching flow rate ratio is:

$$\kappa_2 \geq 1 + 1/\beta \tag{4}$$

where $\kappa_1 = Q_{side1}/Q_{core}$, $\kappa_2 = Q_{side2}/Q_{core}$, $\beta = \eta_{side}/\eta_{core}$, and η is the fluid viscosity. Since for one-phase flow, $\beta = 1$, the theoretical critical flow rate ratio predicted by the model is

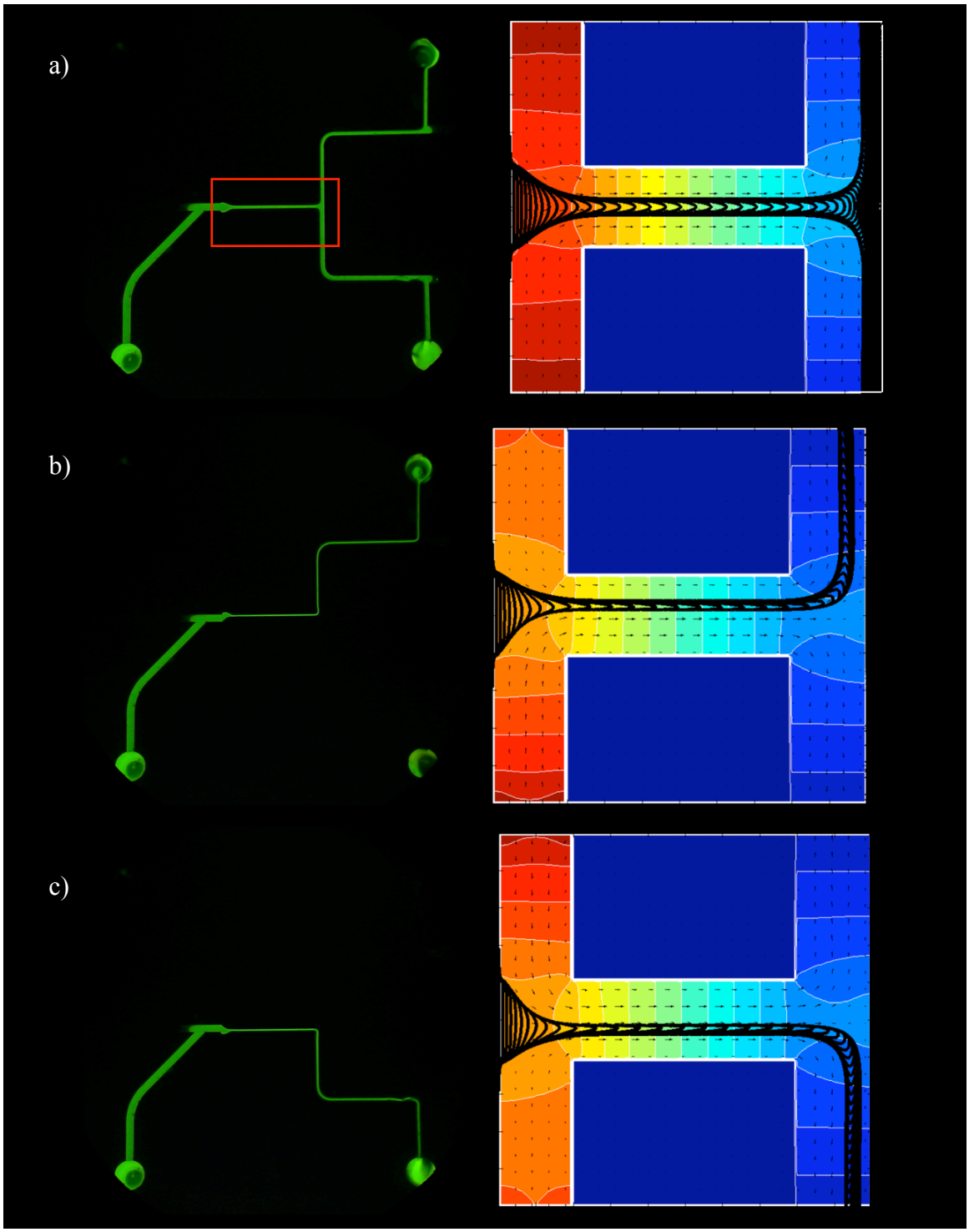

Figure 3-5 Comparison of actual switching results with the results obtained from the finite difference 2-D Navier Stokes model: a) Splitting b) Switched up c) Switched down.

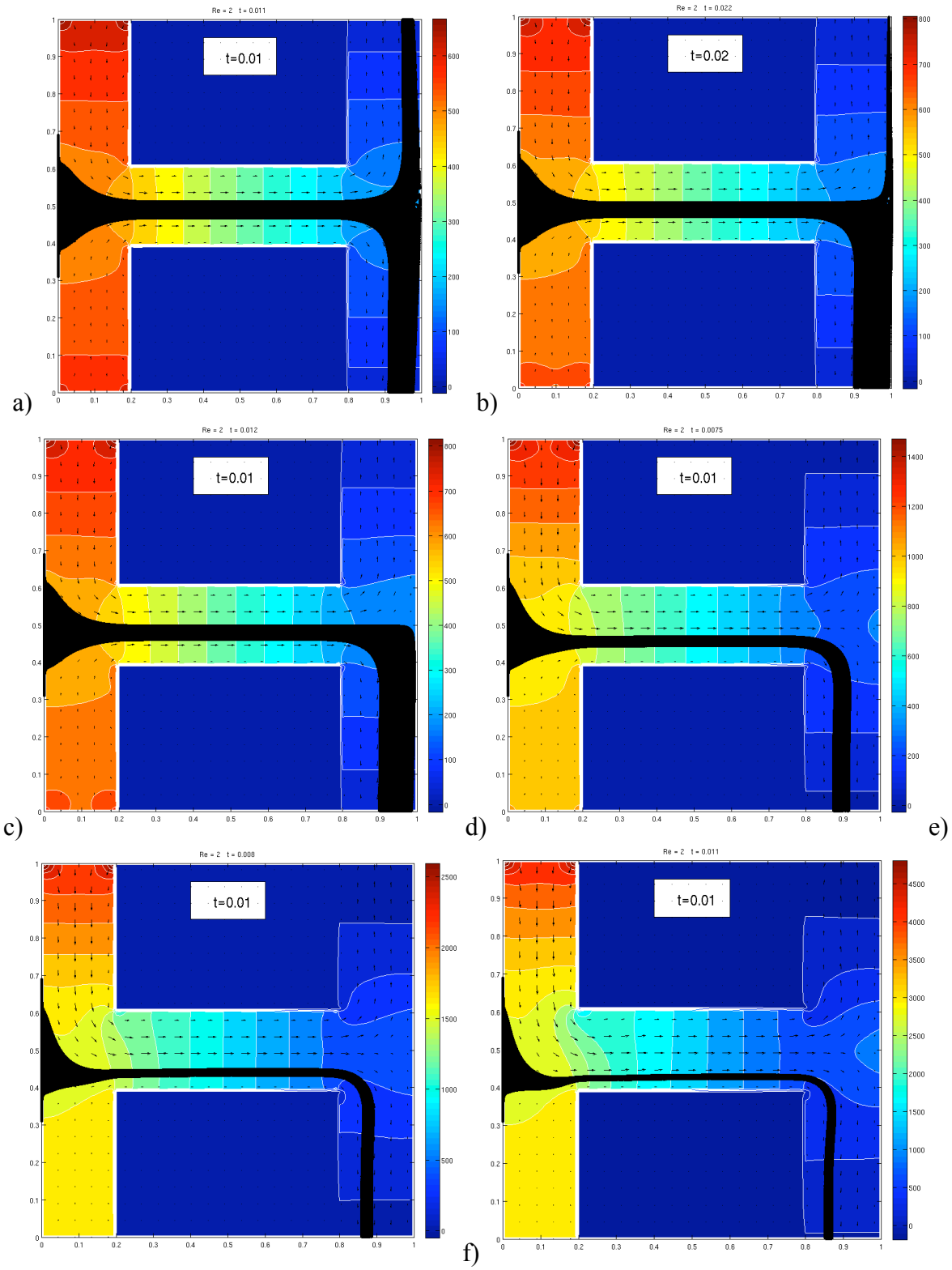

Figure 3-6 The critical flow rate ratio between the side streams is determined to be 2.15:1 (with core speed set to *U=1* and *Re=2*). a) *flow rate ratio = 1.5* b) *flow rate ratio = 2.1 c) flow rate ratio = 2.15 d) flow rate ratio =5 e) flow rate ratio =10 f) flow rate ratio =20*

$\kappa_2 \geq 2$. This means that the theoretical model predicted that for one-phase flow, the critical switching flow rate ratio is 2:1, while the simulation results predict a flow ratio of 2.15:1. In other words, the critical flow rate ratio predicted by theoretical formulation and numerical simulation are in accordance to each other.

3.2.2 Switching Signal

In the experiment, the light signal from the dye solution is measured by a photodiode coupled with optical fiber. I choose to count the number of points that are in the red box region shown in Figure 3-7. The top signal is defined as the number of points that has entered the red box region at the top outlet, while the bottom signal measures the number of points at the bottom outlet.

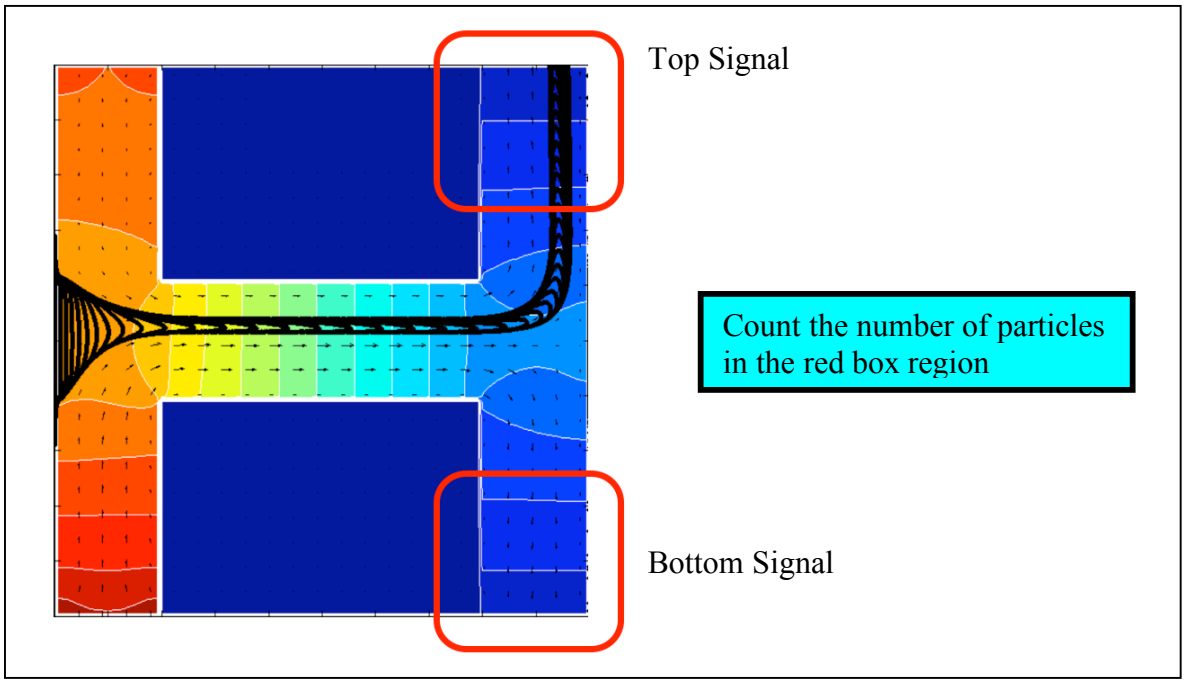

Figure 3-7 The number of particles that entered the red box regions are counted to mimic the signal obtained through fiber optics.

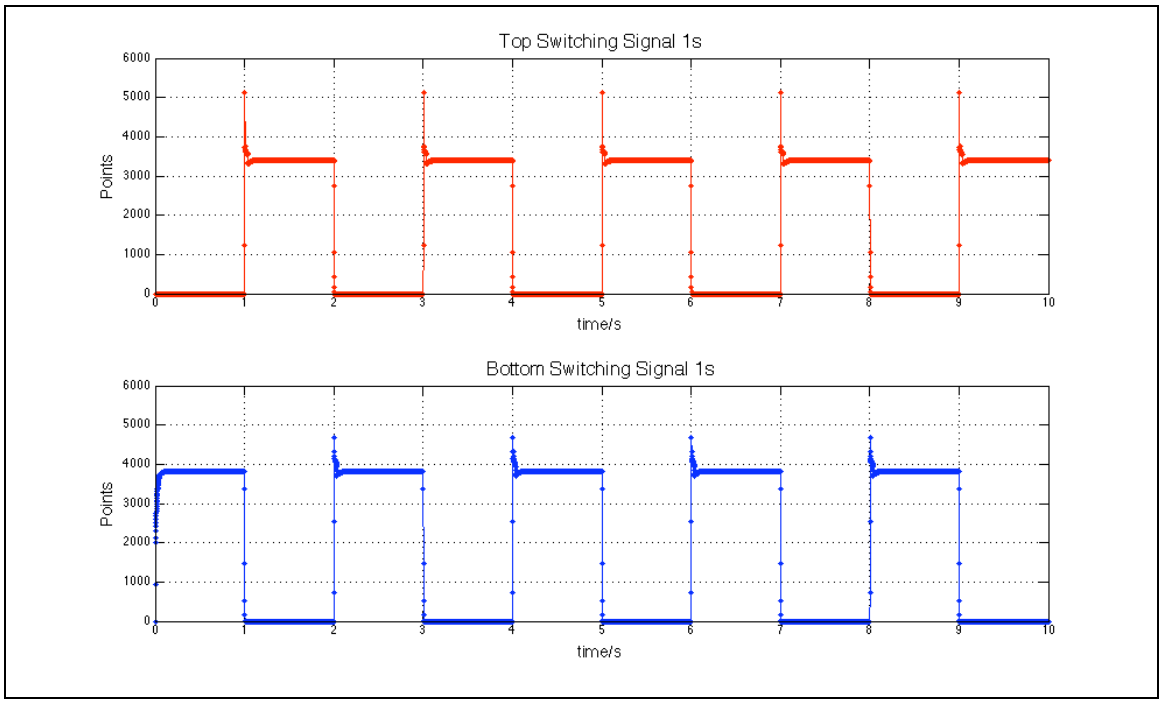

Figure 3-8 Top and bottom signal obtained for one-second switching. There is a sudden increase in number of particles when the two side streams switches flow rates.

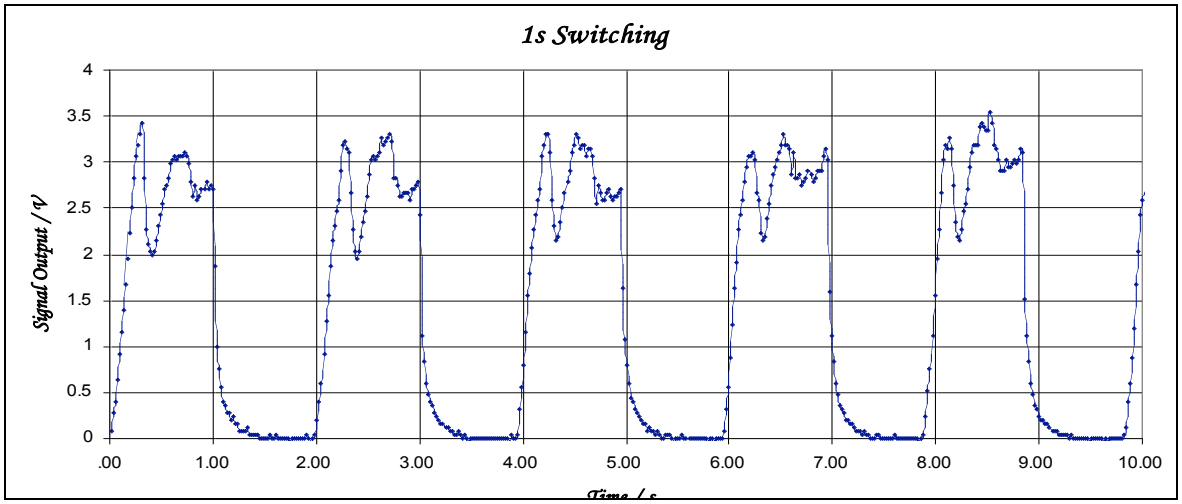

Figure 3-9 One-second switching signal obtained experimentally. Similar trend is observed as compared to simulation results. There is a sudden increase in output voltage during the switching and then the signal is stabilized.

3.2.3 Fastest Switching Speed

It is observed that there is a time lag of about 3 milliseconds (*flow ratio=2.5*) for the particles to reach the other side of the outlet (see Figure 3-10). Hence, I define the fastest switching speed obtainable, for a fix flow ratio of side streams, is the time lag between switching of flow rates and receiving of signal at the other outlet.

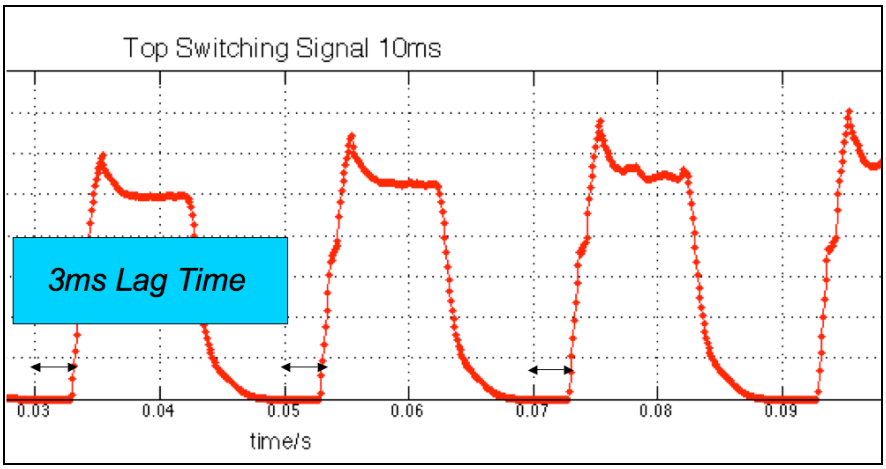

Figure 3-10 Simulation results for 10ms switching. There is a 3ms time lag before the particles reaches the other side of the outlets after the flow rates between the two water side streams are switched.

Figure 3-11 shows the simulation results for 3 millisecond switching. As the particles take 3 millisecond to reach the other outlet, switching at this speed will force the particles to change its direction immediately when they reach an outlet. The fastest switching speed is dependant on the flow rate ratio between the two side streams. Table 3-1 summarizes the fastest switching speed with different sheath stream flow rate ratios. The trend of variation of fastest switching speed with flow rate ratio is shown in Figure 3-12. The fastest switching speed decays exponentially with higher flow rate ratio. The experimental switching speed is restricted by the pump response time. Since the pump response time is about 300ms, the fastest switching achievable physically was 300ms (1.67Hz).

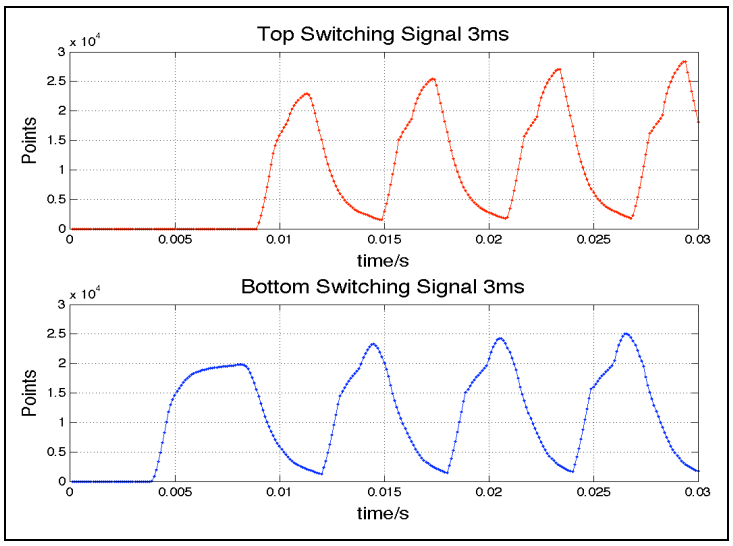

Figure 3-11 Simulation results for 3ms switching. Since there is a lag time of 3ms, the moment the particles reach the other side of the outlet, the flow rates are being swapped and the particles are then forced to change direction again.

Table 3-1 Fastest switching speed variation with flow rate ratio

Speed Difference	Fastest Switching Speed (ms)
2.5	3.0
5.0	1.8
10.0	1.0
20.0	0.1

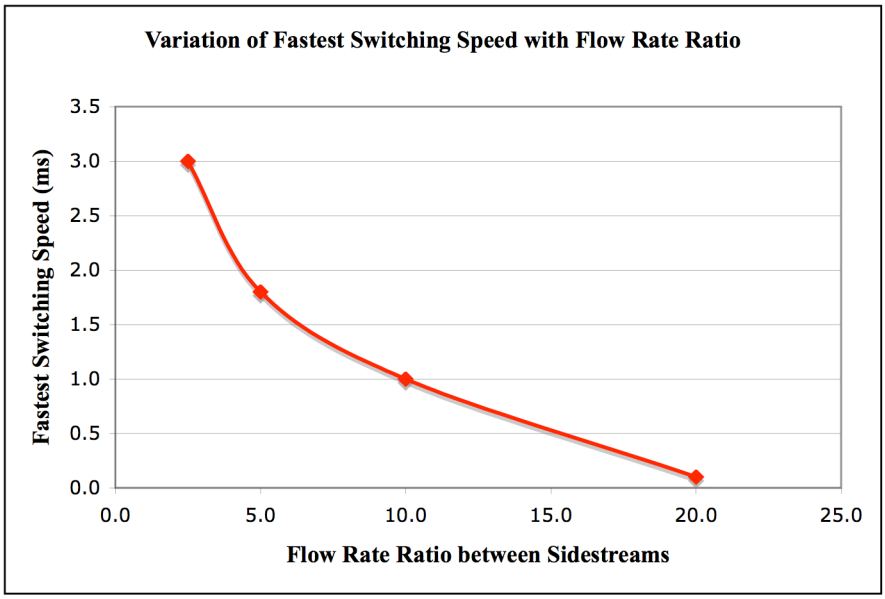

Figure 3-12 Variation of fastest switching speed with flow rate ratio between water sidestreams. The fastest switching speed decreases with higher flow rate ratio.

3.2.4 Switching Pulse

Figure 3-13 shows a variant of the channel design shown in Figure 1-1. Note that instead of having two optical fibers at the top and bottom of the channel, the fiber is placed at the center to record the pulses generated during the sweeping motion of the fluorescent core flow.

Figure 3-14(a) shows the simulated result for one-second switching, while Figure 3-14(b) shows the switching pulses obtained experimentally. Pulses are observed during the swapping of flow rates between sidestreams. However, the pulses are less prominent for faster switching speed. In the numerical simulation, the number of particles in the center of the T-junction are recorded.

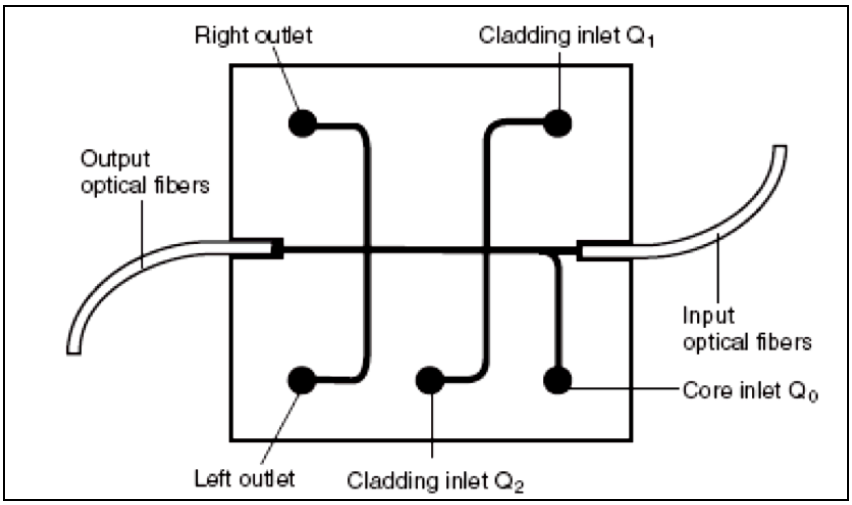

Figure 3-13 A variant of the channel configuration shown in Figure 1-1. The optical fiber is placed in the middle (instead of two fibers at the top and bottom outlet) [1]

a)

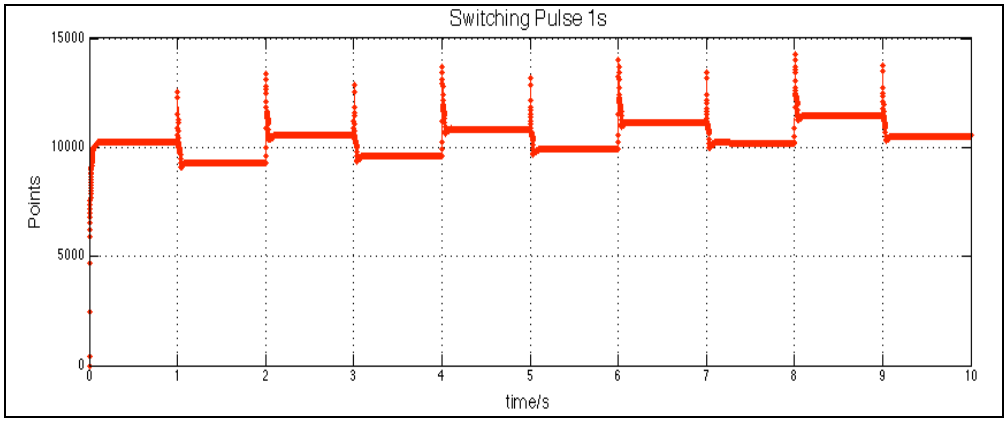

b)

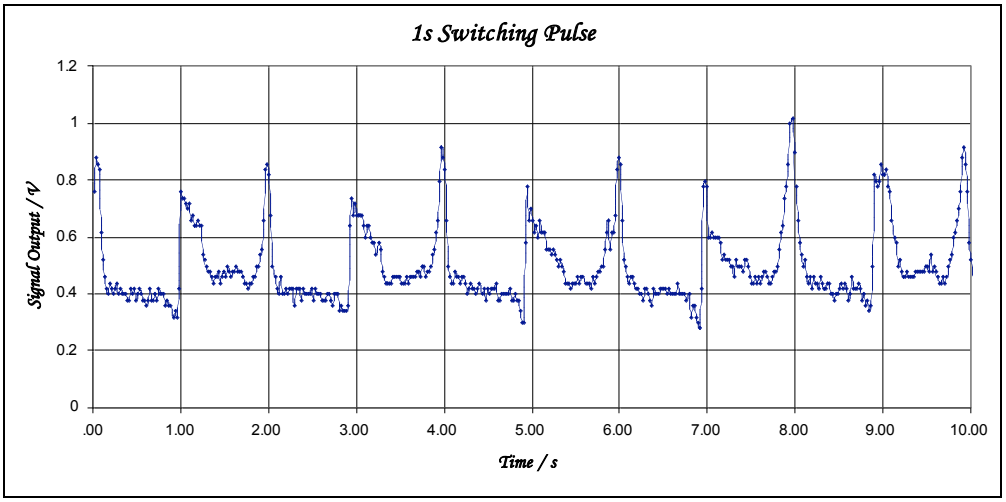

Figure 3-14 a) Simulated switching pulse for one-second switching. There exists distinct sharp spike at the moment of switching. b) Data for switching pulse obtained experimentally.

3.3 Signal Generator

The channel configuration shown in Figure 3-13 can also be used as a microfluidic signal generator. The core width ratio is defined as the ratio of core width to the channel width (Figure 3-15). The signal detected by the fiber optic at the center of the channel is proportional to the core width ratio. Hence, the light intensity output detected by the fiber can be manipulated dynamically through varying the core width ratio.

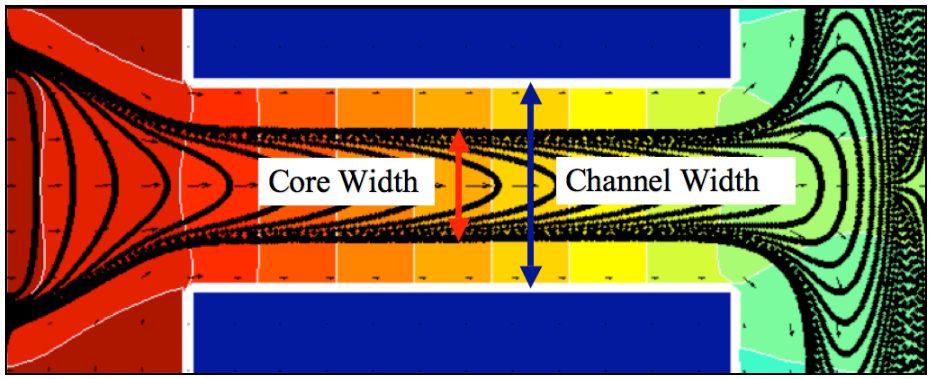

Figure 3-15 Core width ratio is defined as the ratio of core width to the channel width

The theoretical variation of core width ratio with flow rate ratio between the core-sheath streams is given by equation (3). Figure 3-16 shows the theoretical and simulated core width ratio variation with Q_{core}/Q_{side}. The core width ratio grows rapidly with Q_{core}/Q_{side} initially. The width ratio then grows asymptotically to 1 for higher value of Q_{core}/Q_{side}. The core width ratio predicted by simulation is lower than the ratio obtained from the theoretical formulation. This could possibly due to numerical roundoff, or too low grid resolution. For all the simulation results obtained for this project are for $nx = 112$ and $ny = 112$. Furthermore, the Navier Stokes code is only first order accurate.

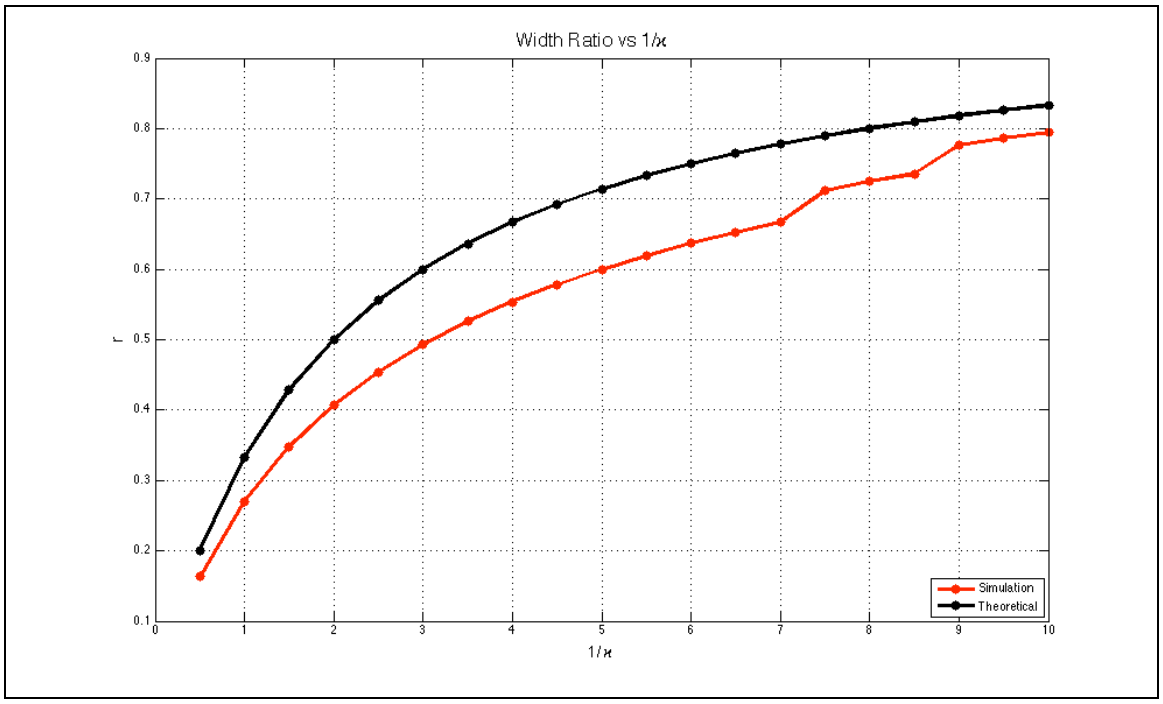

Figure 3-16 Theoretical and simulated core width ratio variation with Q_{core}/Q_{side}

A polynomial curve fitting is done for the simulated result curve (Figure 3-17). The Q_{core}/Q_{side} ratio required for achieving a particular core width ratio (which determines the signal obtain by the fiber) can be read off from the figure. For example, in order to vary the core width ratio as a square wave between $r = 0.3$ and $r = 0.6$, the required Q_{core}/Q_{side} ratios are 0.6 and 4.53, respectively.

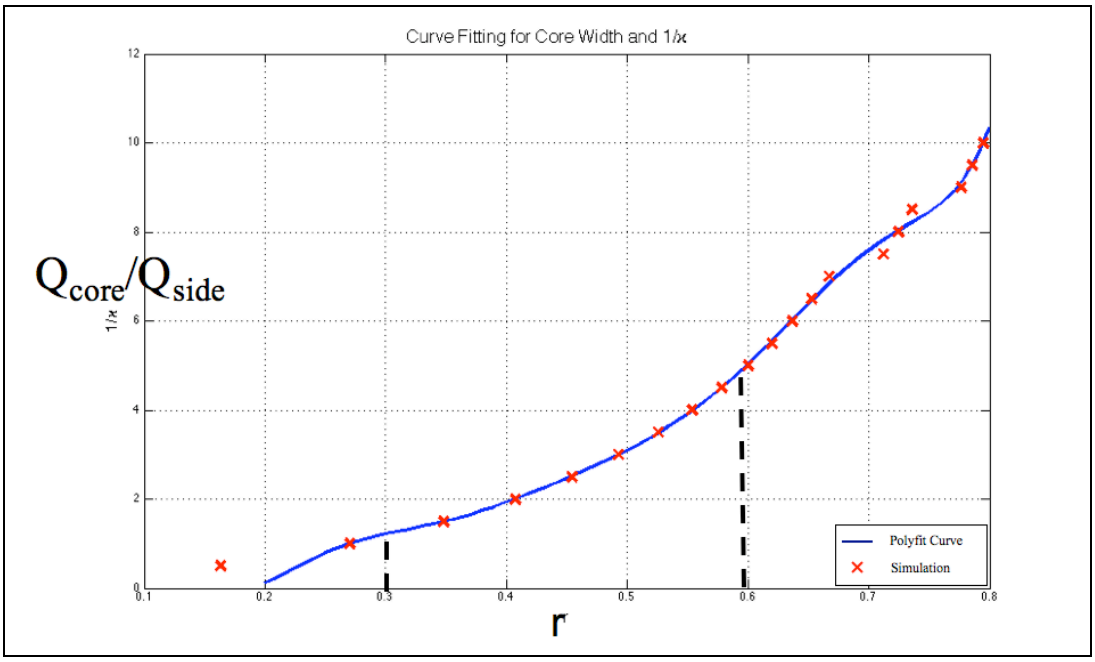

Figure 3-17 A polynomial curve fitting for the simulated data. The Q_{core}/Q_{side} ratio required for a certain core width ratio (which determine the magnitude of signal) can be read off from this graph.

Figure 3-18 shows the comparison of the desired and simulated variation of core width ratio. Indeed, the simulated width ratio variation is close to the desired pattern (sine, square wave, and ramp). The error could be contributed by the fact that the polynomial curve fitting is not perfect as only a small number of data points were used for the characterization of that curve.

Figure 3-19 shows the experimental data for manipulation of core width ratio for a) sine wave, b) square wave, and c) ramp. Although the output does follow the variation of the core width ratio variation patter, there error is much larger compared to the simulation results. Figure 3-20 shows the experimental characterization of the signal obtained with Q_{core}/Q_{side} ratio. The large variation in signal has cause the 'inverse' problem, to manipulate core width ratio, difficult.

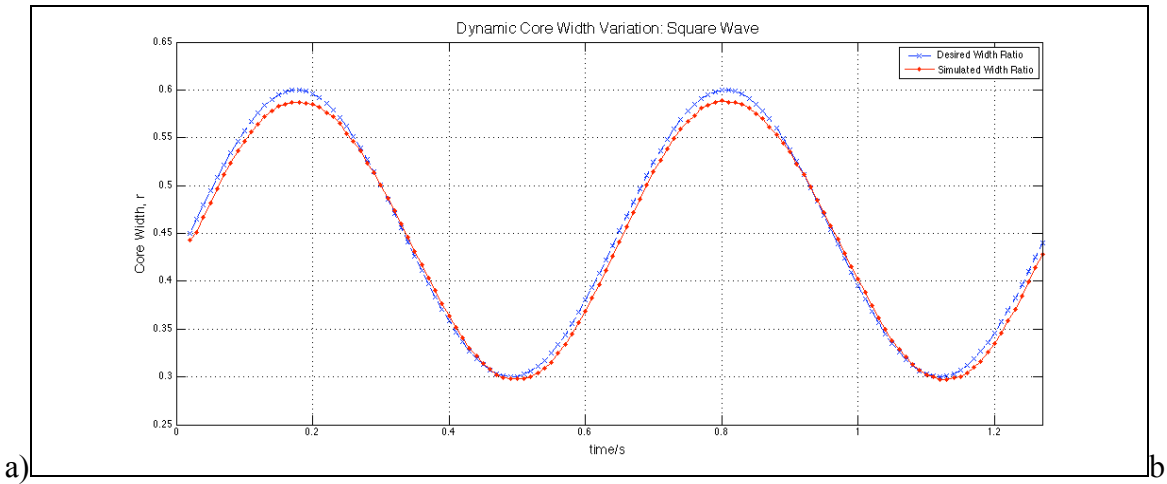

a) b

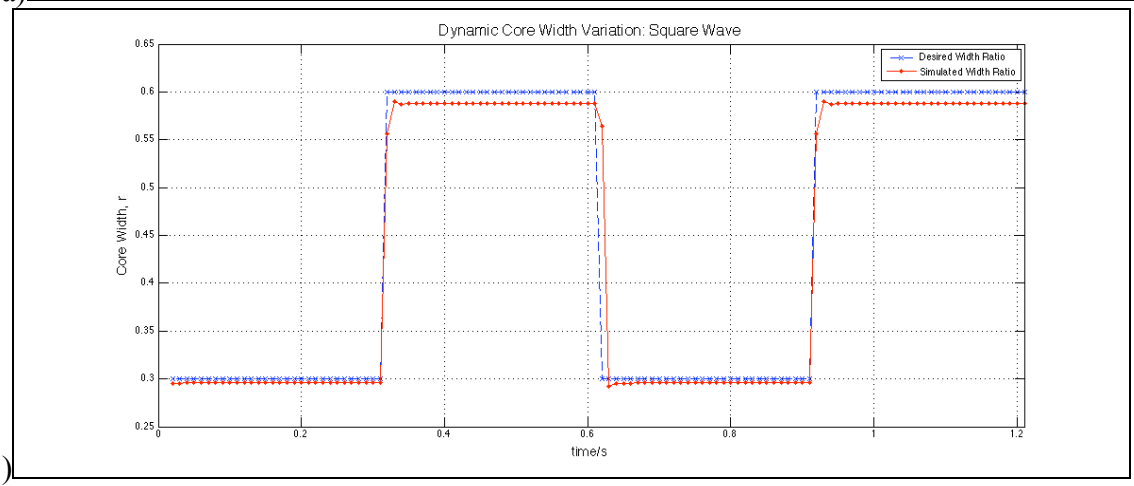

)

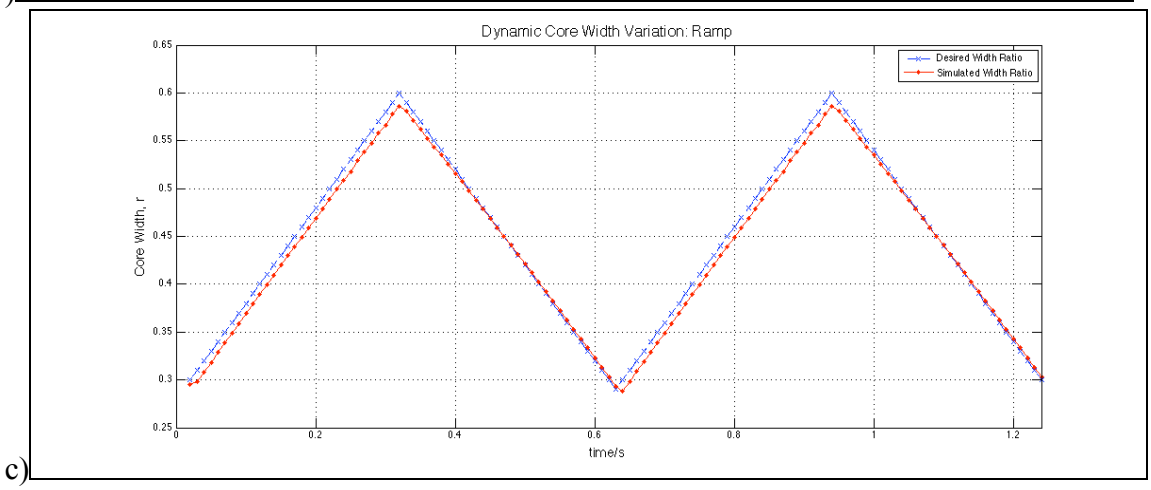

c)

Figure 3-18 Comparison of desired and simulated core width ratio variation for a) Sinusoidal b) Square wave c) Ramp. The simulated variation of the core width ratio is close to the desired variation.

a)

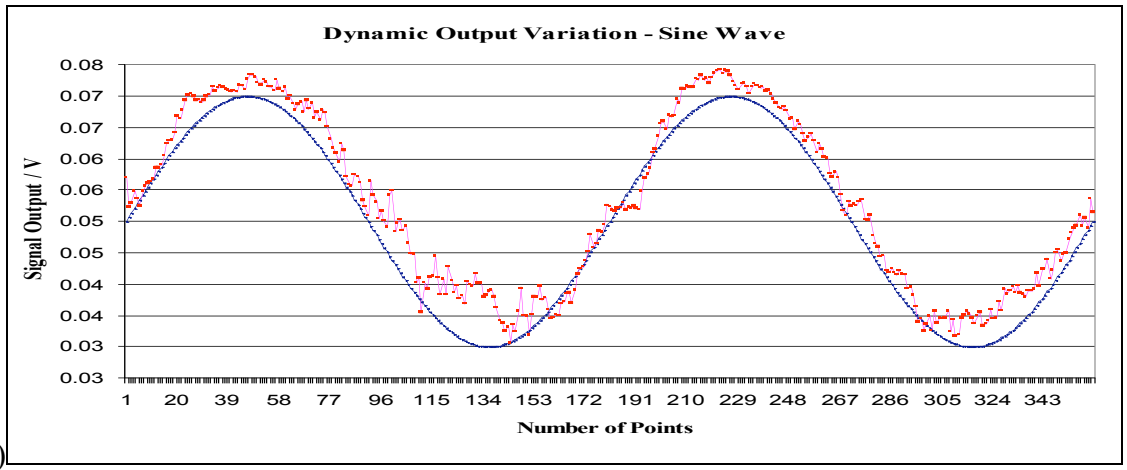

b)

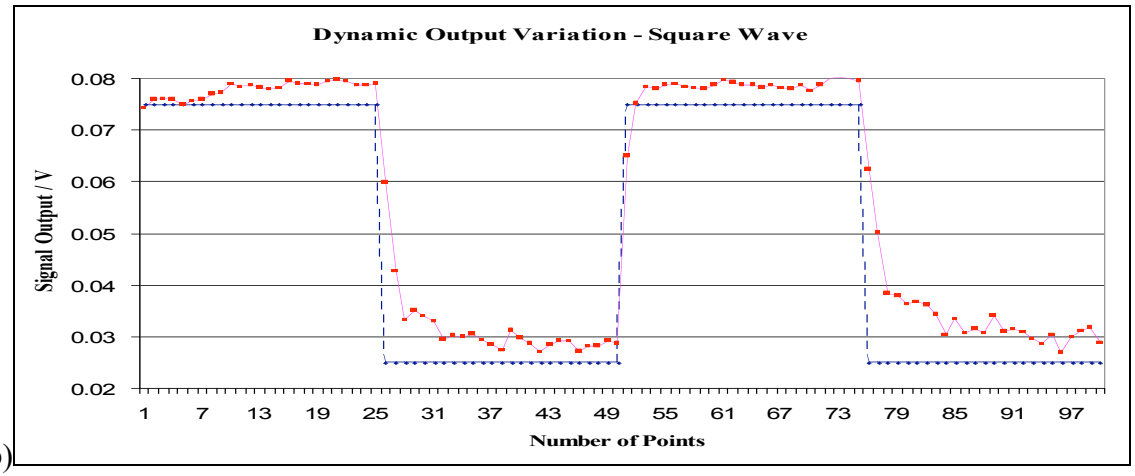

c)

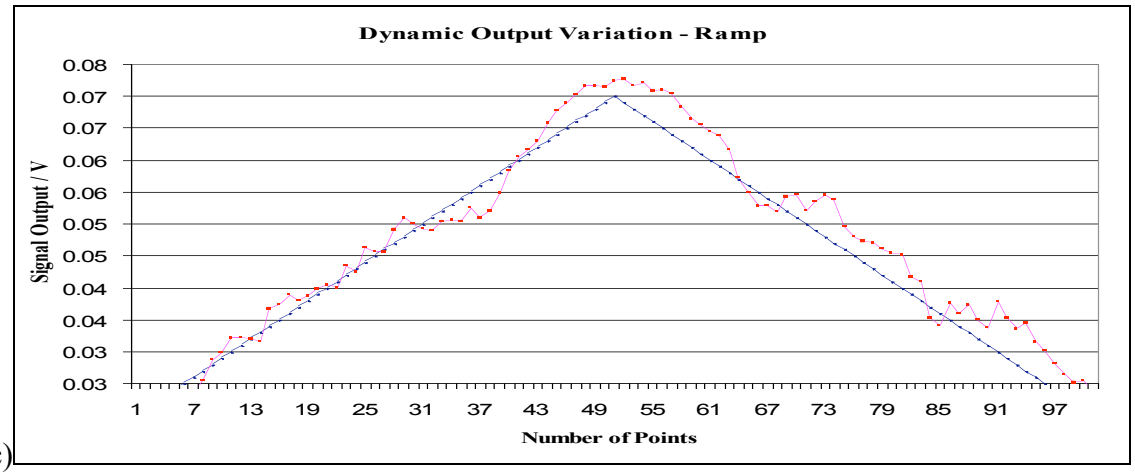

Figure 3-19 Experimental data obtained (through optical fiber) for the core width ratio varying in a) sine wave, b) square wave, c) ramp pattern.

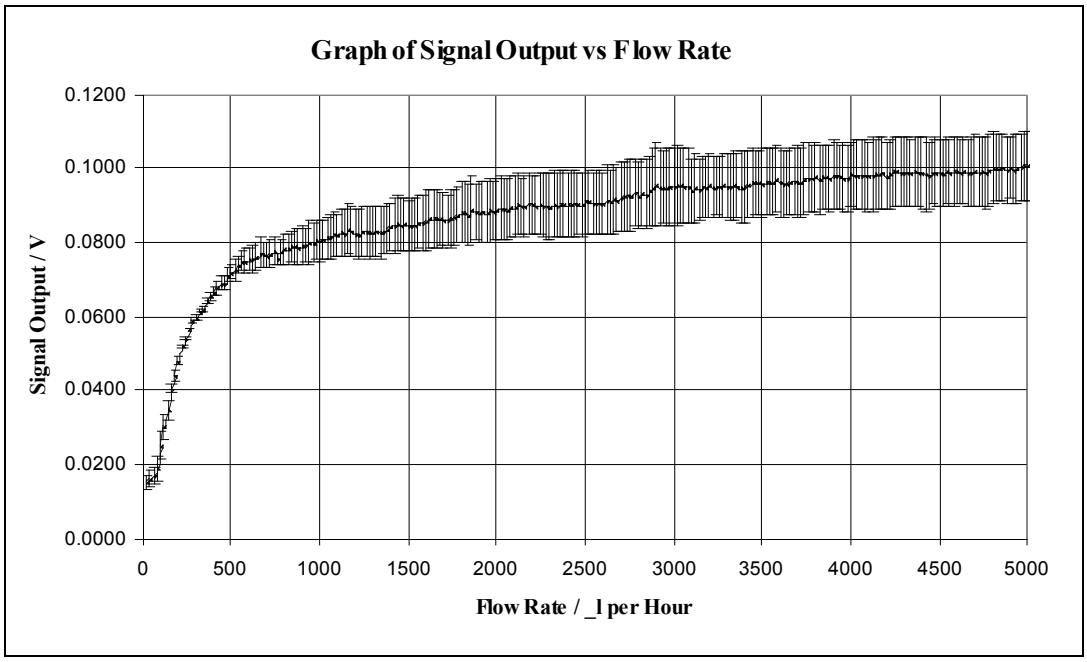

Figure 3-20 Experimental characterization curve of signal output with Q_{core}/Q_{side} .

CHAPTER 4

Conclusion

In this project, we have successfully implemented a finite difference 2-D incompressible Navier Stokes model to simulate the switching behaviors of a microfluidic switch. The critical switching flow rate ratio between the two side streams was found to be 2.15:1 which is very close to the ratio predicted by theoretical model. In addition, the fastest switching speed was found to be dependent on the inlet flow conditions. Generally, the fastest switching speed is about a few millisecond. The fastest switching achieved for real experiment is about 300 milliseond, which is restricted by syringe pump response time.

Finally, dynamic manipulation of signal output was achieved by manipulating core width ratio. The corresponding core width ratio with core-side flow rate ratio can be read off the polynomial fitted characteristic curve. The simulation results for sine wave, square wave, and ramp core width variation were very encouraging.

Recommendation for Future Work

This project can be further extended to include a two-phase flow problem by using level set method. The simulation results for critical switching flow rate ratio between sidestreams for different core-sheath fluid viscosity can be used to verify the theoretical formulation given in [1].

References

[1] Nam-Trung, N, Tian-Fook, Kong, Jun-Hui,Goh, Cassandra, L, "Micro optofluidic splitter and switch based on hydrodynamic spreading". Journal of Micromechanics and Microengineering.

[2] Zhigang, W; Nam-Trung, N, "Hydrodynamic focusing in microchannels under consideration of diffusive dispersion: theories and experiments". *Sensors and Actuators B (Chemical)*, v 107, n 2, 29 June 2005, p 965-74.

[3] Benjamin Seibold, "A compact and fast Matlab code solving the incompressible Navier-Stokes equations on rectangular domain," November 2007, http://www-math.mit.edu/cse/codes/mit18086_navierstokes.pdf.